Terawatt to Petawatt Subpicosecond Lasers

Michael D. Perry and Gerard Mourou

The application of the chirped-pulse amplification technique to solid-state lasers combined with the availability of broad-bandwidth materials has made possible the development of small-scale terawatt and now even petawatt (1000-terawatt) laser systems. The laser technology used to produce these intense pulses and examples of new phenomena resulting from the application of these systems to atomic and plasma physics are described.

Over the past few years a revolution has occurred in our ability to produce extremely high-power and high-intensity pulses. Ten years ago, a tabletop system with a beam size on the order of a centimeter could typically produce gigawatt pulses. The same size system today can now produce pulses with over 1000 times this peak power and achieve focused irradiance greater than 10^{18} W/cm^2. This ability opens for study a whole new regime of laser-matter interaction, with applications in fusion, relativistic plasma physics, x-ray generation, and many other areas. The increase in peak power and irradiance is the direct result of the technique of chirped-pulse amplification (CPA) (*1, 2*). A chirped pulse is one where the frequency of the electromagnetic field varies with time. First Q-switching, then mode locking, and now CPA have all resulted in dramatic increases in peak power (Fig. 1). With CPA, pulses exhibiting power near the theoretical limit can in principle be achieved.

The CPA technique makes possible efficient energy extraction from high energy-storage materials by short pulses without incurring nonlinear effects associated with high intensity. The rapid progress in peak power has largely been the result of our ability to generate and manipulate these short pulses and amplify them in a wide variety of broadband solid-state materials: Nd:glass (*1–4*), alexandrite (5), Ti:sapphire (*6, 7*), Cr:LiSrAlF$_6$ (LiSAF) (*8, 9*), and combinations of these materials (*10*). The CPA technique has also been applied to existing, large-scale Nd:glass systems at the CEA (Commissariat a l'Energie Atomique) Limeil in France (*11*), the Rutherford-Appleton Laboratory in Great Britain, and at Osaka in Japan (*12*). To date, pulses with peak power exceeding 55 TW (25 J, 400 fs) have been produced at CEA Limeil. At Lawrence Livermore National Laboratory (LLNL), the construction of a 1000-TW (petawatt) system is under way.

M. D. Perry is with the Laser Program, Lawrence Livermore National Laboratory, P.O. Box 808, L-493, Livermore, CA 94551, USA. G. Mourou is at the Center for Ultrafast Sciences, University of Michigan, Ann Arbor, MI 48109, USA.

By producing short pulses only after amplification, CPA increases the extractable energy from broadband materials to a level achievable with long (nanosecond) pulses. As a result, not only can the peak power of short-pulse systems be dramatically increased, but also their average power. The original dye- or excimer-based picosecond lasers typically had an average power of 10 to 100 mW (Fig. 2). With CPA, the higher energy density of solid-state materials is accessible for these short-pulse lasers, resulting in systems with average power on the order of 1 W, approaching that of conventional longer pulse solid-state systems. The average power limit has not been reached, and we expect that in the near future femtosecond amplification systems will produce an average power at the 10-W level. High average power is desirable for applications in high harmonic generation (*13*), ultrafast spectroscopy (*14*), medicine (*15*), and imaging (*16, 17*).

The production of a pulse with high peak power is a necessary but not sufficient condition to produce a high-irradiance pulse. The brightness and ultimate focused irradiance achievable with a laser pulse is determined by both the peak power and the spatial quality (divergence) of the pulse. By paying careful attention to both linear and nonlinear aberrations in the laser and beam-transport systems, one can now produce nearly diffraction-limited, multiterawatt pulses. When focused, such pulses can achieve irradiance between 10^{18} and 10^{19} W/cm^2. Scaling these CPA-based systems up to the 100-TW or even petawatt level will enable the study of laser-matter interaction at 10^{21} W/cm^2 and beyond.

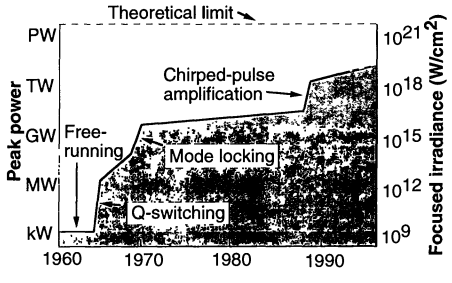

Fig. 1. Increase in peak power and focused irradiance of small-scale (area, 1 cm^2) lasers.

The availability of these intense pulses opens a new regime of laser-matter interaction for study. Applications stem from four fundamental features of such a pulse. The first is simply the short duration, which makes possible experiments with a resolution of 100 fs or less and, in plasma applications, virtually eliminates hydrodynamic motion during the laser pulse (*18, 19*). Second are the large electric and magnetic fields associated with an intense pulse. At 10^{21} W/cm^2, the resulting electric field is 10^{14} V/m, over 100 times the Coulomb field that binds atomic electrons. This field strength is sufficient to ionize heavy atoms such as uranium to U^{82+} within the short duration of the pulse (Fig. 3). Third is simply the energy density and resulting light pressure of the pulse. At 10^{21} W/cm^2, the energy density of the pulse is over 3×10^{10} J/cm^3, which corresponds to a 10-keV blackbody and an equivalent light pressure of 300 Gbar. Finally, the free electrons produced by these intense pulses are driven by the field to a cycle-averaged oscillatory energy given by

$$E_{osc} = mc^2(\sqrt{1 + 2U_p/mc^2} - 1) \quad (1)$$

where m is the electron mass, c is the speed of light, $U_p = e^2E^2/4m\omega^2 = 9.33 \times 10^{-14} I\lambda^2$ is the nonrelativistic oscillatory energy

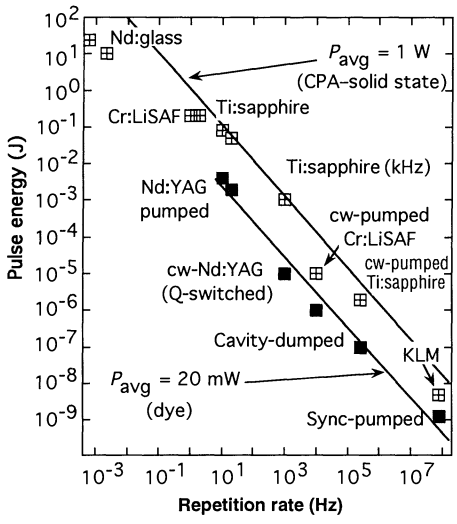

Fig. 2. Current average power (P_{avg}) of femtosecond lasers (cw, continuous wave; YAG, yttrium-aluminum-garnett; KLM, Kerr lens modelocked; Cr:LiSAF, chromium-doped LiSrAlF$_6$; synch, synchronous).

of a free electron (measured in electron volts if the laser intensity I is in watts per square centimeter and the wavelength λ is in micrometers), e is the electron charge, and ω is the laser frequency. For a Nd:glass laser producing 1.05-μm laser pulses, the electron quiver energy (Fig. 4) is nearly 10 MeV for a laser intensity of 10^{21} W/cm^2. Relativistic effects in such a plasma become dominant and can result in new absorption mechanisms (*20, 21*), including absorption past the critical surface (*22*) and self-focusing (*23*), not observed in conventional laser-plasma experiments.

The Chirped-Pulse Amplification Technique

As the pulse duration decreases from the nanosecond to the picosecond and femtosecond regimes, it becomes increasingly difficult to extract the stored energy from a laser amplifier without causing detrimental nonlinear effects. This arises from the fact that the input fluence necessary to efficiently extract the stored energy has to be on the order of the saturation fluence, $F_{sat} = h\nu/\sigma$, where h is Planck's constant, ν is the laser frequency, and σ the emission cross section. The saturation fluence of most solid-state laser materials is between 1 J/cm^2 (Ti:sapphire) and 6 J/cm^2 (Nd:glass). Amplification of picosecond pulses to this level is not possible because of the intensity-dependent index of refraction $n = n_0 + n_2 I$, where I is the intensity of the pulse. This intensity-dependent refractive index produces a nonlinear phase retardation given by

$$B = \frac{2\pi}{\lambda} \int_0^l n_2 I(z) dz \qquad (2)$$

where l is the propagation length. This nonlinear phase retardation results in wavefront distortion and eventually catastrophic filamentation (*24*), which causes damage to the amplifier. For example, a picosecond pulse amplified to 1 J/cm^2 could travel only 1 mm through a typical solid-state laser material without suffering severe degradation of beam quality.

Before the advent of CPA, picosecond and femtosecond pulses were produced from dye- and excimer-based systems. The effects on the nonlinear refractive index were unimportant in these systems because they could only produce pulses with a peak power of a few gigawatts per square centimeter as a result of their low energy storage capability (F_{sat} = 1 mJ/cm^2 for dyes and 5 mJ/cm^2 for excimers). To access the several-joules-per-square-centimeter capability of solid-state materials, a femtosecond pulse must be stretched by a factor of several thousand before amplification. It is then amplified by a factor of 10^6 to 10^{10} and recompressed ideally to its initial value (Fig. 5). Like other laser techniques (including the laser itself, Q-switching, and mode locking), the microwave-CPA analog was demonstrated more than 40 years ago for radar (*25*). By stretching the pulse before amplification, researchers could achieve high pulse energy for long-distance ranging. Recompression of the echo produced the short pulses necessary for accuracy. In most CPA systems in the optical regime, the pulse is recompressed directly after amplification. However, the complete analog to the radar systems has been recently demonstrated in the optical regime for long-range, high-accuracy LIDAR (light detection and ranging) by Braun *et al.* (*26*).

The CPA technique in the optical regime requires impressive manipulation. First, a very short (femtosecond) and high-contrast pulse is generated at the nanojoule level. Second, this pulse is stretched by a factor of up to 10^4. Third, it is amplified by 10 to 11 orders of magnitude. Fourth, it is recompressed by a factor of 10^4 to near its initial value. The end result is ideally a diffraction-limited pulse with an extremely high contrast ratio.

Generation of short and ultraclean pulses. It is now possible to produce pulses as short as 10 fs (*27*) with the Kerr lens effect in Ti:sapphire oscillators (*28*). Although these pulses are extremely short, they have the tendency to exhibit a tail that extends over a few hundred femtoseconds before the peak of the pulse. For some experiments, it is necessary to eliminate this tail. A high-

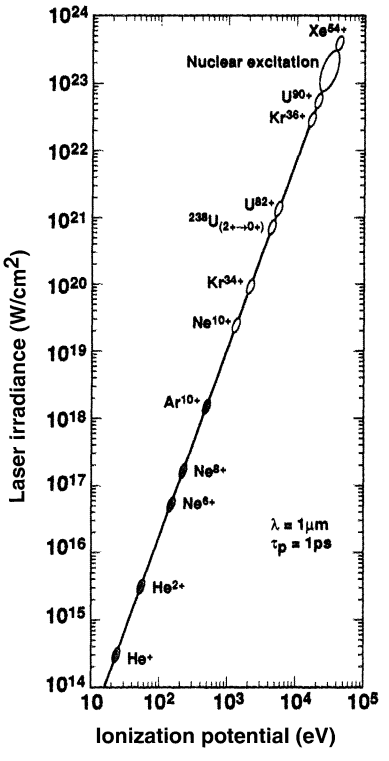

Fig. 3. Charge states accessible by means of tunneling ionization with a picosecond laser pulse at 1053 nm. The solid circles represent charge states formed by laser field ionization that have been observed to date.

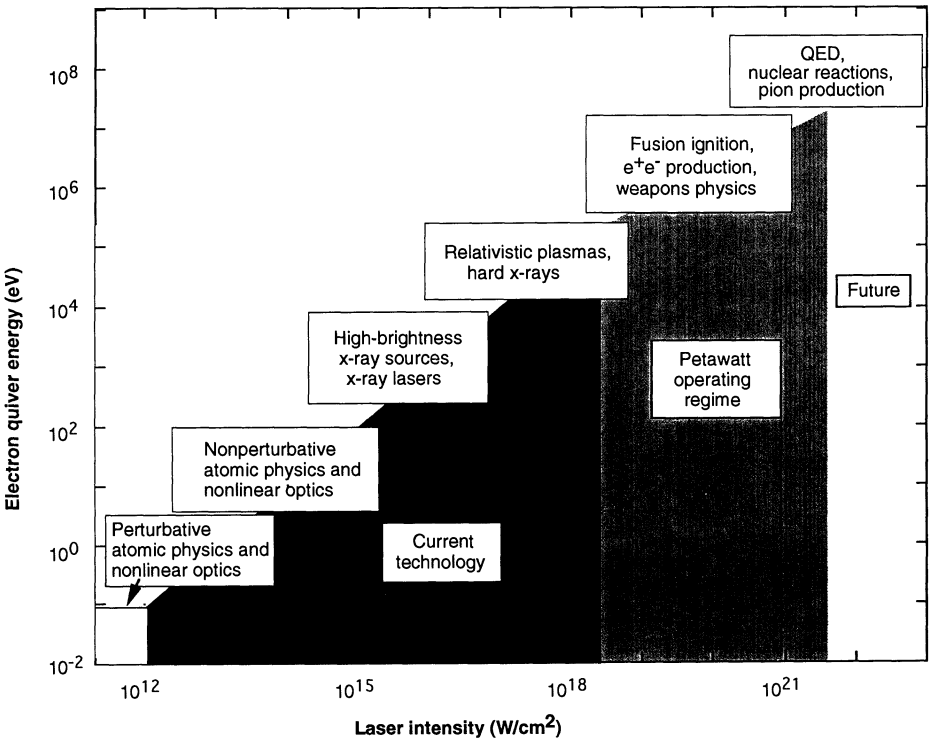

Fig. 4. Electron quiver energy and accessible phenomena as a function of laser irradiance (λ = 1053 nm) (QED, quantum electrodynamics; e^+e^-, positron-electron pair).

contrast pulse cleaner that uses cross-phase modulation in a single-mode fiber located between two crossed polarizers is one technique to eliminate this pedestal. With this technique, a contrast enhancement of six orders of magnitude has been obtained (*29*).

Stretching. After generation, the short pulse is passed through a pulse stretcher exhibiting a frequency-dependent phase function, $\beta(\omega)$. This produces a chirped and stretched pulse. A chirped pulse is one that exhibits a time-dependent frequency. In the first optical CPA demonstration (*1*), group velocity dispersion in fiber was used to stretch the pulse. The lower frequency (red) components of the pulse propagate faster through the fiber than the higher frequency (blue) components, resulting in a stretched and positively chirped (red earlier than blue) pulse. Recompression was performed with the negative group velocity dispersion provided by a diffraction grating pair (*30*).

With CPA systems based on fiber gratings, the grating separation is adjusted to cancel the positive dispersion of the fiber, correct to second order. The residual error in the compressed pulse is primarily the result of the mismatch in the third-order dispersion between the grating pair and material dispersion in the fiber. The maximum compression ratio, R, that can be produced by these fiber-grating systems is of the order of $\Delta\lambda/\lambda$. When R exceeds this value, incomplete recompression is performed, producing unwanted ripples before or after the main pulse. For example, a picosecond pulse at 1.06 μm with a $\Delta\lambda$ of 20 Å cannot be stretched and compressed by more than a factor of 500 with fiber-grating systems. For a 100-fs pulse, fiber-grating systems are limited to $R \approx 50$.

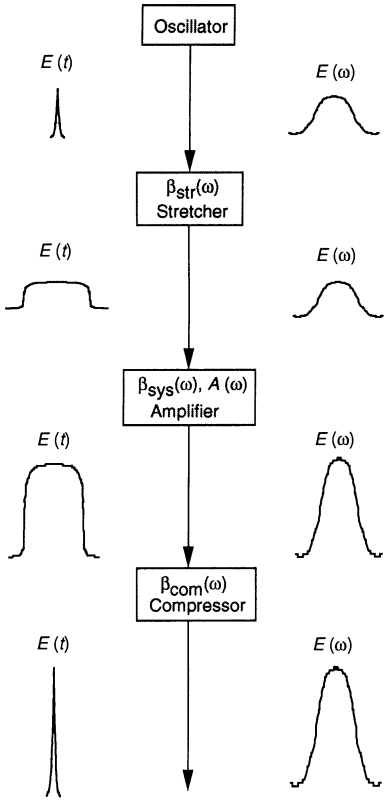

Fig. 5. Chirped pulse amplification concept. The waveforms $E(t)$ and $E(\omega)$ represent the time- and frequency-dependent field distribution; $\beta(\omega)$ and $A(\omega)$ are the frequency-dependent phase and amplitude transfer functions, respectively, of a given component of the laser system.

In 1987, Martinez proposed a compressor with positive group velocity dispersion to compress pulses at 1.5 μm (*31*). In this regime, the fiber has negative group velocity dispersion and the pulses exhibit a negative chirp. Recompression of the pulses requires a device with positive group velocity dispersion. His compressor was a telescope with a magnification of one between two antiparallel diffraction gratings. Unlike the fiber, this positive-dispersion "compressor" acted as a pulse stretcher matched to the negative dispersion grating pair over all orders. Pessot *et al.* (*32*) first demonstrated this all-grating stretching-compression system by stretching an 80-fs pulse to over 80 ps ($R > 1000$) and then recompressing the pulse without introducing any temporal distortion. The matched stretcher-compressor was a breakthrough. A number of groups quickly demonstrated stretching and compression to 10^4. Several techniques are being examined to further improve the ratio to over 10^5 (*33, 34*).

Amplification and gain narrowing. Short pulses have a large Fourier spectrum that is modified by the amplitude transfer function $A(\omega)$ of the amplifier system. Because of the large overall gain involved in CPA, typically 10^{10}, the spectrum of the amplified pulse is significantly narrower than the material bandwidth (*4*). For a material exhibiting a Gaussian lineshape, the spectrum is reduced to a width (full width at half maximum) (*35*)

$$\Delta\omega = \Delta\omega_a \sqrt{\frac{3}{G(\omega_a) - 3}} \qquad (3)$$

where $\Delta\omega_a$ is the material gain bandwidth and G is the gain in decibels. From this expression, we see how important it is to work with materials having a large gain bandwidth, such as Nd:glass, alexandrite, Ti:sapphire, Cr:LiSAF, or a combination of these. A reduction in gain bandwidth not only reduces the stretched pulse duration but also results in a longer pulse after compression.

Compression. A perfectly matched stretcher-compressor will have conjugate phase functions, $\beta_{str}(\omega) = -\beta_{com}(\omega)$. However, for the very large stretching and amplification required to produce terawatt pulses, the phase function of the compressor must account for the sum of the phase functions of the stretcher and the remainder of the laser system, $\beta_{sys}(\omega)$, including amplifiers, mirrors, and waveplates. Writing the field of the pulse exiting the compressor as

$$E_{out}(\omega) = E_{in}(\omega)A(\omega)\exp\{i[\beta_{str}(\omega) + \beta_{sys}(\omega) + \beta_{com}(\omega)]\} \qquad (4)$$

we see that a transform-limited pulse is achieved after compression only if $\beta_{com}(\omega) = -[\beta_{str}(\omega) + \beta_{sys}(\omega)]$. In this case, the amplified and compressed pulse has no residual chirp, $\delta = [\beta_{com}(\omega) + \beta_{str}(\omega) + \beta_{sys}(\omega)] = 0$, and the temporal distribution of the field is just the Fourier transform of the spectrum of the field. In practice, the grating separation in the compressor is adjusted until the error, δ, is a minimum.

Petawatt pulses. The features of all high-power CPA-based laser systems are observable in the design of the petawatt laser (Fig. 6) under development at LLNL. The laser begins with a self-mode–locked Ti:sapphire oscillator producing 90-fs pulses at 1053 nm. These low-energy (~5 nJ), transform-limited pulses are stretched by a factor of 12,000 to 1.2 ns in a single-lens, single-grating pulse stretcher. After stretching, the pulse energy is reduced to 500 pJ. This low-energy pulse is injected into a Ti:sapphire regenerative amplifier. The Ti:sapphire is used as the gain medium at this stage to avoid the gain narrowing associated with Nd:glass regenerative amplifiers (*36*). This transverse electromagnetic mode 00 regenerative amplifier serves as a multipass amplifier and ensures diffraction-limited beam quality. Over 100 passes through the gain medium are required to achieve an amplification of over 10^7 at 1053 nm. The regenerative amplifier routinely produces 6-mJ pulses with less than 3% fluctuation in output energy (*37*). After the regenerative amplifier, the pulse makes eight passes through a Ti:sapphire power amplifier, increasing the pulse energy to 50 mJ.

Unfortunately, amplification in Ti:sapphire beyond the 100-mJ level at wavelengths beyond 1 μm is impractical because of the cost and complexity of laser pumping. Further amplification to the 2-J level is achieved in a pair of flashlamp-pumped 19 mm by 200 mm LG-760 Nd:glass amplifiers. This 2-J beam can then be compressed for use in small-scale experiments or coupled into the Nd:glass power amplifier chain. This amplifier chain is a modified section of a beamline of the Nova laser at LLNL. The low-energy chirped pulse is spatially filtered and injected into the disk amplifier chain with about 50% coupling and is expected to produce 1.6 kJ at the output of the 31.5-cm disk amplifiers (a typical Nova beamline has an additional amplifier stage and produces 10 kJ in a 1-ns pulse).

This beam is then expanded to 40 cm before pulse compression.

Perhaps the most challenging component of the petawatt laser is the compression and focusing of a multikilojoule, subpicosecond pulse. To compress the 1.6-kJ pulse to under 500 fs requires the production of high-efficiency, 60 cm by 110 cm diffraction gratings with a damage threshold exceeding 1.5 J/cm^2. The largest high-efficiency diffraction gratings commercially available are 25 cm by 40 cm metallic gratings with a diffraction efficiency as high as 92% and a damage threshold greater than 250 mJ/cm^2 for 300-ps pulses. At LLNL, we have developed gold gratings with over 96% diffraction efficiency and a damage threshold over 400 mJ/cm^2 for 300-ps pulses (38). However, even this improved damage threshold for metallic gratings is insufficient. For this reason, we embarked on a new approach for reflection gratings based on dielectric materials, which in theory would yield both high diffraction efficiency and extremely high damage thresholds (39). To date, we have produced ZnS-based diffraction gratings with a diffraction efficiency above 96% at 1053 nm and a damage threshold above 1 J/cm^2 for 500-ps pulses. Production of these gratings in oxide-based materials is estimated to increase the damage threshold to over 3 J/cm^2 for 500-ps pulses, enabling the compression of multikilojoule pulses.

Planned to be fully operational in 1995, the petawatt laser is designed to deliver a 1-kJ pulse at 1053 nm in a beam 40 cm in diameter. The pulse is designed to be tunable between 500 fs and 20 ps and to be focusable to twice the diffraction limit in a *f*/3 focusing system, producing a focused irradiance well above 10^{21} W/cm^2. The pulse will be synchronized with the other beams of the Nova laser to better than 10 ps.

Table 1. Theoretical peak power.

Laser type	Cross section (10^{-20} cm^2)	$\Delta\lambda$ (nm)	τ (fs)	P_{th} (TW/cm^2)
Nd:glass phosphate	4	22	80	60
Nd:glass silicate	2.3	28	60	100
Nd:glass combination	1.5	60	30	400
Ti:sapphire	30	120	8	120
Alexandrite	1	100	10	2000
Cr:LiSAF	3	50	15	300

Theoretical peak power. Even the petawatt laser is below the theoretical limit of peak power. This limit can be estimated as the ratio of the extractable energy (approximated by the saturation fluence) to the minimum pulse duration imposed by the gain bandwidth (neglecting gain narrowing). The peak power limit P_{th} per unit area, assuming a time-bandwidth product $\Delta\nu_a\,\Delta\tau = 0.5$, is then estimated by

$$P_{th} = 2\,F_{sat}\,\Delta\nu_a \qquad (5)$$

This power also represents that needed to produce a Rabi oscillation in the amplifying medium. The theoretical peak power for different materials is estimated in Table 1. In principle, 100-TW pulses are achievable with compact systems, and even exawatt (1 EW = 10^{18} W) pulses are possible with large-aperture (1-m) Nd:glass systems that contain a mixture of silicate and phosphate glasses to maximize the gain bandwidth. These high-power CPA-based systems will be limited by the technology required to stretch and compress pulses with a power density greater than 10^{13} W/cm^2.

Applications

The application of tabletop terawatt lasers to problems in a wide range of physics and chemistry has been as rapid as the development of the laser technology. Here, we

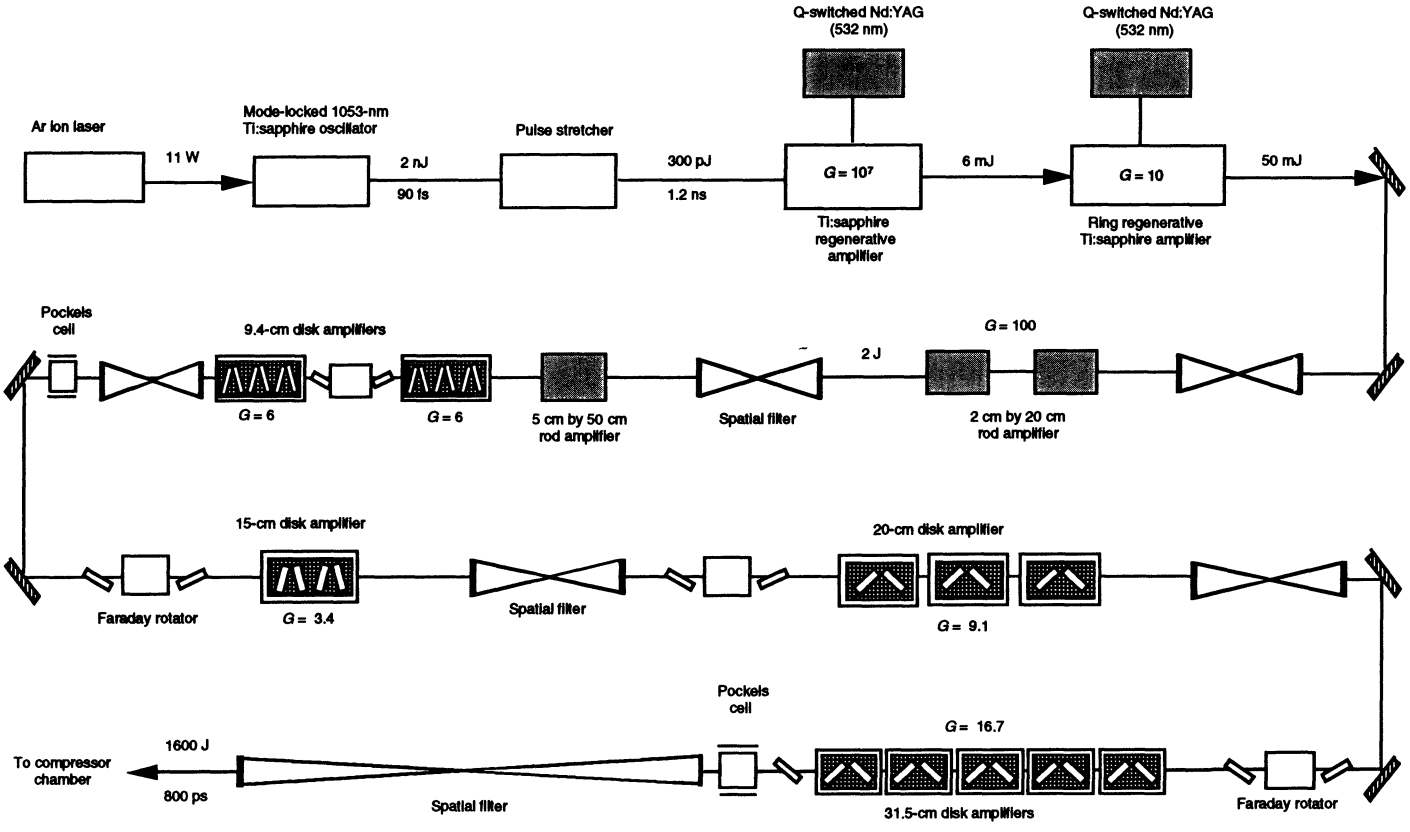

Fig. 6. Schematic of the petawatt laser currently under development.

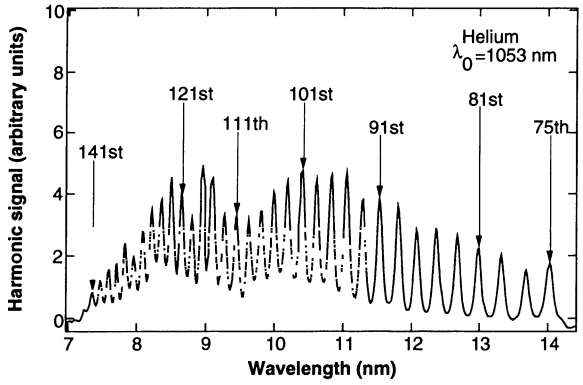

Fig. 7. Harmonic spectrum resulting from the interaction of intense (10^{16} W/cm^2) 1053-nm radiation with helium.

introduce a few of the recent developments in atomic and plasma physics and nonlinear optics as an attempt to illustrate phenomena accessible with terawatt and petawatt subpicosecond lasers.

Atomic physics and nonlinear optics of bound electrons. Several experiments on multiphoton ionization (*40–42*) and above-threshold ionization (*43–46*) coupled with numerous theoretical calculations (*47–50*) showed that beyond about 10^{13} W/cm^2, multiphoton absorption phenomena can no longer be described by conventional perturbation theory. This "nonperturbative" behavior results from the fact that the electric field of the laser is approaching that of the Coulomb field and the oscillatory energy, U_p, of the free electron is comparable with or even exceeds the electron binding energy. Only a few years ago, complicated dye (*51*) or excimer (*52*) amplifier systems were necessary to perform these experiments. The availability of CPA-based subpicosecond lasers has eliminated the need for these complex systems and accelerated the revolution in this area of atomic physics.

Although there are several emerging applications of this nonperturbative phenomenon, here we will concentrate on the production of coherent extreme ultraviolet (XUV) and soft x-ray radiation by high-order harmonic generation (*13, 53*). The generation of odd harmonics to as high as the eleventh, resulting from the interaction of moderate-intensity ($<10^{11}$ W/cm^2) laser radiation with dense gases, had been well established (*54*). However, by shortening the pulse duration to avoid ionization and increasing the intensity, researchers have observed harmonics extending to the 109th of 811-nm radiation (*55*) and the 143rd of 1053-nm radiation (*56*) (Fig. 7).

These harmonics result from the periodic oscillation of quasi-free electrons across the atomic potential. As the electron passes the nucleus, it suffers an impulsive distortion in its trajectory that generates a broad spectrum of radiation. In a quantum picture, the harmonics can be understood as multiphoton excitation far into the continuum (absorption of N photons) with emission of a single photon of energy $Nh\nu$ returning the electron to the ground state. The maximum kinetic energy of those oscillating electrons that have a trajectory that returns them to the vicinity of the nucleus, and hence the maximum energy available for harmonic emission, is approximately $IP + 3U_p$ (*57*), where U_p is the cycle-averaged quiver energy (Eq. 1). From the λ^2 scaling of the quiver energy, we expect longer wavelength lasers to produce much shorter wavelength harmonic radiation in good agreement with the experimental observations (*58*).

Because the harmonics are produced only by the driving field of the laser, their duration is limited by the short duration of the laser pulses. In a streak-camera recording of harmonic radiation and recombination fluorescence resulting from the interaction of short (600 fs), intense (10^{16} W/cm^2) 527-nm radiation with dense helium gas (Fig. 8) (*59*), the harmonics appear as bright spots at $t = 0$, unresolved by the picosecond resolution of the streak camera.

Both the coherence and the overall conversion efficiency are limited by phase matching between the harmonic field and the incident laser field (*60*). If the focused beam has a depth of field, b, much longer than the length of the nonlinear medium, L, low-divergence harmonic beams with a near-Gaussian spatial distribution can be produced (*61*). Production of XUV harmonic radiation near 20 nm (25th harmonic of 526-nm incident radiation) with an absolute conversion efficiency as high as 10^{-7} has recently been reported (*62*). Longer wavelength radiation (>50 nm) can be produced with a conversion efficiency exceeding 10^{-6} with the use of xenon as the nonlinear medium (*60*). In an application of this high-order harmonic radiation, we have measured the photoionization cross section of neon from 20 to beyond 100 eV (*63*). Previous measurements made in the XUV spectral region required large synchrotron facilities or intense plasma discharge sources.

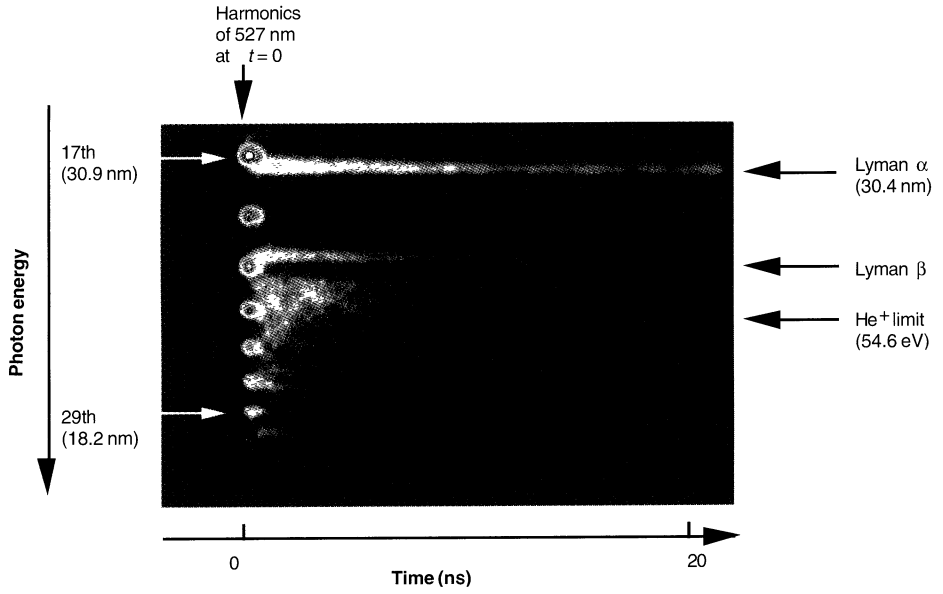

Fig. 8. Time-resolved emission from a helium plasma produced by 600-fs, 527-nm pulses. Emission from the 17th to 31st harmonics is unresolved by the streak camera, and the Lyman series following recombination occurs over several nanoseconds (*59*).

High-Temperature, High-Density Plasmas

Similar to the observation of a host of new phenomena in laser-atom interaction above 10^{13} W/cm^2, as the $I\lambda^2$ product approaches and exceeds 10^{18} W μm^2/cm^2, new phenomena are expected in the interaction of these intense laser pulses with plasmas. At 10^{18} W μm^2/cm^2, the cycle-averaged quiver energy of free electrons is 100 keV, requiring relativistic corrections to many basic plasma parameters. Phenomena such as rel-

ativistic self-focusing (*23*), emission of terahertz radiation (*64*), wake-field generation (*65*), and strongly coupled scattering (*66*) have either been observed or are predicted. In addition, the subpicosecond duration of these pulses leads to transient phenomena that result in short-duration, high-brightness x-ray emission (*18, 67*). Here, we introduce only a few recent observations on hot electron generation and the resulting x-rays produced.

Hard x-ray emission. Hard (>100 keV) x-rays produced by hot electron bremsstrahlung had been observed numerous times in laser-plasma experiments with long (>100 ps) pulses, particularly with CO_2 lasers (*68*). The majority of these experiments produced hot electrons by stimulated Raman scattering at and below critical density in the plasma. For short, intense pulses, the production of hot electrons is governed by other mechanisms. Collisions in the high-density plasmas produced by short pulses tend to rapidly thermalize the quiver energy, producing quasi-Maxwellian plasmas with a temperature characterized by the free electron quiver energy (*22*). The first experiments to show evidence of hot electron generation with short pulses were performed by Kmetec *et al.* (*69*), who observed the emission of megaelectron volt x-rays at $I\lambda^2 \approx 10^{18}$ W $\mu m^2/cm^2$. Direct measurement of megaelectron volt electrons followed (*70*). The hard x-ray bremstrahlung spectrum is well fit by a single Maxwellian distribution (Fig. 9A) and is in reasonable agreement with the quiver (ponderomotive) energy (Fig. 9B).

Light pressure at the critical surface. In conventional plasmas, light penetration past the density at which the plasma frequency $\omega_{pe} = [4\pi e^2 n_e/m_e]^{1/2}$ is equal to the frequency of the laser pulse is evanescent. The plasma density at this point is known as the critical density, and the laser pulse is reflected at the critical surface. However, at the intensities available with short-pulse terawatt lasers, the light pressure can be larger than the thermal pressure of the plasma and the laser pulse can modify the plasma profile, penetrating past the critical surface (*22*). This effect was inferred by Liu and Umstadter (*71*) from observations of a reduction of the plasma thermal expansion when the laser intensity exceeded 5×10^{16} W/cm^2.

Solid-density plasmas. Solid-density (>10^{23} electrons per square centimeter) plasmas with kilovolt temperatures exist only in the interior of stars or inertially confined plasmas. However, short, intense (~10^{18} W/cm^2) pulses of extremely high contrast can produce extremely hot, near–solid-density plasmas by interacting with a solid target. Because of the short duration and high contrast of the pulse, a near–solid-density plasma is formed before the plasma can expand and cool. This was recently demonstrated in a set of experiments by Kieffer *et al.* with a 2-TW, 0.5-μm laser pulse (400 fs) focused on a solid aluminum target at intensities up to $I\lambda^2 = 10^{18}$ W $\mu m^2/cm^2$ (*73*). In Fig. 10A, we show the time-integrated $1s2l2l'$-$1s^22l$ line spectrum of Li-like aluminum irradiated with a 1-μm pulse at 4×10^{18} W/cm^2 with a several-nanosecond-long prepulse at 8×10^{12} W/cm^2. This line spectrum indicates strong non-Maxwellian and nonstationary effects and is typical of an interaction between a subpicosecond pulse and a preformed plasma having a gradient scale length of a few laser wavelengths. Figure 10B shows the time-integrated Li-like spectrum obtained when the target is irradiated with a high-contrast, 0.5-μm pulse at 10^{18} W/cm^2 (prepulse suppression caused by frequency doubling). The line shape and line broadening (*72, 73*) indicate that this Li-like emission (effective atomic number $Z^* = 10$) is produced at an electron density of 4×10^{23} cm^{-3}. This behavior, which is not expected from scaling laws based on the thermal expansion of the plasma, indicates the presence of a strong radiation pressure of a few hundred megabars.

Inertial confinement fusion. Conventional inertial confinement fusion (ICF) relies on the formation of a hot central core within the dense fuel to spark ignition. This condition is achieved by the rapid, highly symmetric, spherical implosion of the capsule driven by temporally shaped multinanosecond pulses delivered either directly by a multitude of laser beams or indirectly by x-rays. Because of the extreme requirements on symmetry and the necessity to achieve both high temperature and density in the implosion, conventional ICF requires substantial energy from the laser to achieve ignition and fusion burn (*74*) of the deuterium-tritrium (D-T) fuel (Fig. 11).

In 1991, work began on a new concept to ignite the compressed D-T fuel in an ICF implosion. The concept requires the delivery of an intense, multikilojoule pulse to the dense, imploded fuel within a few picoseconds (*75*). The "fast ignition" concept decouples compression from ignition and thereby substantially reduces the requirements both on implosion symmetry and

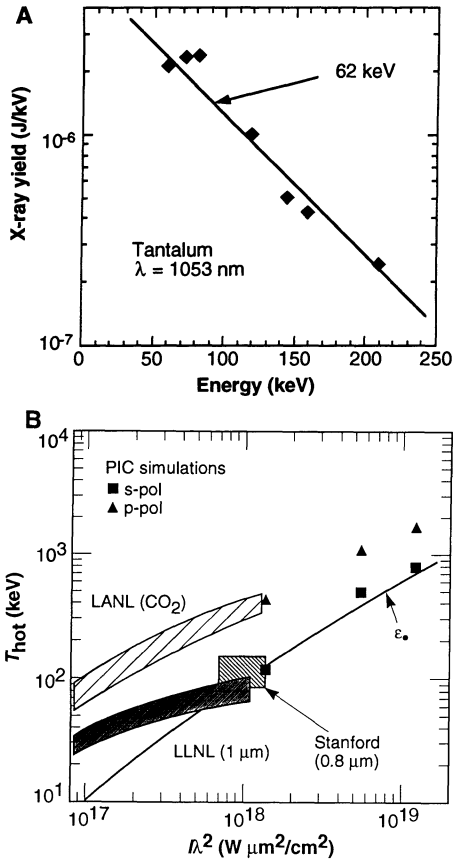

Fig. 9. (**A**) Hard x-ray spectrum from the interaction of a 600-fs, 1053-nm laser pulse at 5×10^{17} W/cm^2 with a thick Ta target. (**B**) Predicted (*22*) and measured (*70*) electron temperature near the critical surface. The squares and triangles are the result of simulations for s-polarized (squares) and p-polarized (triangles) radiation; the solid line is the quiver energy of a free electron (Eq. 1). LANL, Los Alamos National Laboratory.

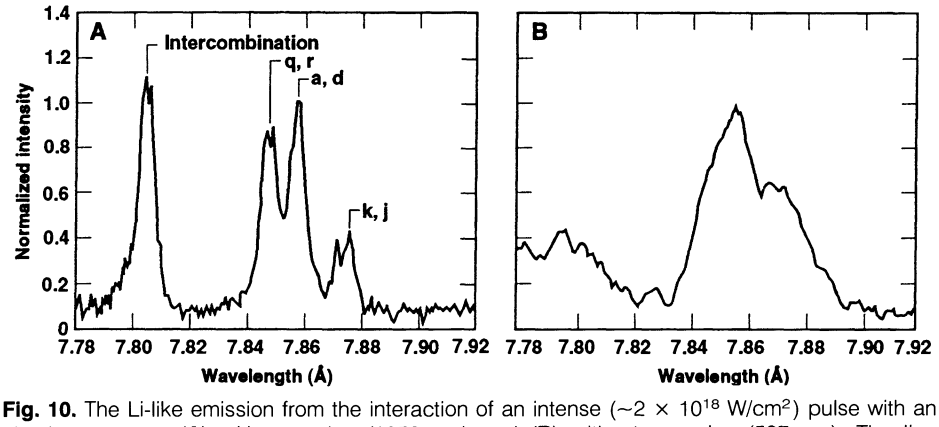

Fig. 10. The Li-like emission from the interaction of an intense (~2×10^{18} W/cm^2) pulse with an aluminum target: (**A**) with prepulse (1053 nm) and (**B**) without prepulse (527 nm). The line broadening indicates a plasma density of 4×10^{23} cm^{-3}. [From Kieffer *et al.* (*73*)]

laser energy necessary to achieve target gain (Fig. 11). Instead of relying on a shock-heated central core, the essential idea is to assemble the fuel with sufficient density to sustain fusion burn but with a low and uniform temperature (a few hundred electron volts). At the point of maximum compression, the ion temperature is rapidly increased to ignition conditions (5 to 10 keV). The "heat" is injected by relativistic electrons (~1 MeV) produced by the interaction of intense ($>10^{20}$ W/cm^2) laser light with plasma at and beyond critical density. The electrons deposit their energy through collisions in the dense fuel.

The electrons must be produced and deposit their energy before the compressed fuel can disassemble. A dense D-T plasma of effective radius $\langle R \rangle$ will disassemble in a time on the order of $\langle R \rangle / c_s$, where c_s is the sound speed. Simple calculations, supported by detailed LASNEX (*76*) numerical modeling, show that the time for disassembly of the compressed fuel is on the order of 50 ps but decreases to less than 10 ps as the fuel is heated. On the other hand, the electron-ion equilibration time, τ_{ei}, is on the order of a picosecond. Balancing pellet disassembly with electron-ion equilibration dictates that the ignitor pulse be between 1 and 10 ps.

Relative to the solid foundation of conventional ICF, the "fast ignition" concept is still in its infancy and relies on many of the phenomena associated with relativistic laser plasmas that are only now being addressed. The petawatt laser described previously is being developed to test the fast ignition concept and provide a facility for the investigation of laser plasma phenomena at values of $I\lambda^2$ to 10^{21} W μm^2/cm^2 and beyond.

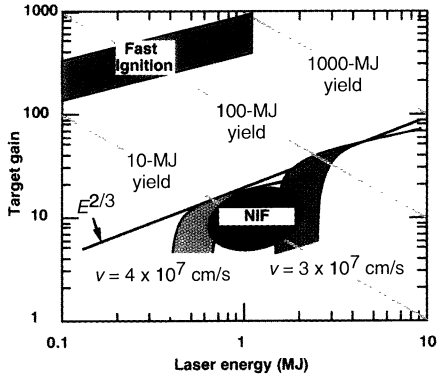

Fig. 11. Predicted fusion gain of an indirectly driven deuterium-tritrium capsule as a function of 351-nm laser energy. The lower curves represent the gain achieved in convention ICF at different implosion velocities (*74*). The upper curve represents the theoretical operating regime of a fast electron ignited capsule (*75*). The operating regime of the proposed National Ignition Facility (NIF) is shown superimposed.

Conclusion

The development of terawatt, and soon petawatt, lasers based on CPA has led to new opportunities in the interaction of intense laser radiation with matter. In this article, we have focused on the enabling laser technology and introduced the application of these sources to atomic and plasma physics. Continuing laser development to produce both high-energy (kilojoule), low–repetition-rate systems and low-energy (millijoule) high–repetition-rate (kilohertz) (*77*) systems will further expand the applications of these powerful new laser sources.

REFERENCES AND NOTES

1. D. Strickland and G. Mourou, *Opt. Commun.* **56**, 219 (1985).
2. P. Maine, D. Strickland, P. Bado, M. Pessot, G. Mourou, *IEEE J. Quantum Electron.* **24**, 398 (1988).
3. M. Ferray *et al.*, *Opt. Commun.* **75**, 278 (1990).
4. M. D. Perry, F. G. Patterson, J. Weston, *Opt. Lett.* **15**, 381 (1990), F. G. Patterson and M. D. Perry, *J. Opt. Soc. Am. B* **8**, 2384 (1991).
5. M. Pessot, J. Squier, P. Bado, G. Mourou, D. Harter, *IEEE J. Quantum Electron.* **25**, 61 (1989); M. Pessot, J. Squier, G. Mourou, D. Harter, *Opt. Lett.* **14**, 797 (1989).
6. J. Kmetec, J. J. Macklin, J. F. Young, *Opt. Lett.* **16**, 1001 (1991).
7. A. Sullivan *et al.*, *ibid.*, p. 1406.
8. T. Ditmire and M. D. Perry, *ibid.* **18**, 426 (1993).
9. P. Beaud, M. Richardson, E. Miesak, B. T. Chai, *ibid.*, p. 1550.
10. W. E. White, J. R. Hunter, L. Van Woerkom, T. Ditmire, M. D. Perry, *ibid.* **17**, 1067 (1992).
11. C. Sauteret *et al.*, *ibid.* **16**, 238 (1991); C. Rouyer *et al.*, *ibid.* **18**, 214 (1993).
12. K. Yamakawa, H. Shiraga, Y. Kato, *ibid.* **16**, 1593 (1991).
13. K. Li, A. L'Huillier, M. Ferray, L. A. Lompré, G. Mainfray, *Phys. Rev. A* **39**, 5751 (1989).
14. J.-L. Martin, A. Migus, G. Mourou, A. H. Zewail, Eds., *Ultrafast Phenomena VIII* (Springer-Verlag, Berlin, 1993).
15. B. Zysset, J. G. Fujimoto, C. A. Puliafito, R. Birngruber, T. F. Deutsch, *Lasers Surg. Med.* **9**, 193 (1989).
16. P. P. Ho *et al.*, *Opt. Photonics News* **4**, 23 (1993), and references therein; L. Wang, P. P. Ho, C. Liu, G. Z. Zhang, R. R. Alfano, *Science* **253**, 769 (1991), and references therein.
17. E. Leith *et al.*, *J. Opt. Soc. Am. A* **9**, 1148 (1992).
18. M. M. Murnane, H. C. Kapteyn, M. D. Rosen, R. W. Falcone, *Science* **251**, 531 (1991).
19. C. Y. Chien *et al.*, *Opt. Lett.* **18**, 1535 (1993).
20. F. Brunel, *Phys. Rev. Lett.* **59**, 52 (1987).
21. P. Gibbon and A. R. Bell, *ibid.* **68**, 1535 (1992).
22. S. C. Wilks, W. Kruer, M. Tabak, A. B. Langdon, *ibid.* **69**, 1383 (1992).
23. P. Sprangle, E. Esarey, A. Ting, *ibid.* **64**, 2011 (1990).
24. Y. R. Shen, *Principles of Nonlinear Optics* (Wiley Interscience, New York, 1984) and references therein; W. Koechner, *Solid-State Laser Engineering* (Springer-Verlag, New York, ed. 3, 1990).
25. C. E. Cook, *Proc. IRE* (1960), p. 310.
26. A. Braun, C. Y. Chien, S. Coe, G. Mourou, in preparation.
27. M. T. Asoki *et al.*, *Opt. Lett.* **18**, 977 (1993).
28. D. E. Spence, P. N. Kean, W. Sibbett, *ibid.* **16**, 42 (1991).
29. J. L. Tapié and G. Mourou, *ibid.* **17**, 136 (1992).
30. E. B Treacy, *IEEE J. Quantum Electron.* **5**, 454 (1969).
31. O. E. Martinez, *ibid.* **23**, 1385 (1987).
32. M. Pessot *et al.*, *Opt. Commun.* **62**, 419 (1987).
33. B. E. Lemoff and C. P Barty, *Opt. Lett.* **18**, 1651 (1993).
34. P. Tournois, *Electron. Lett.* **29**, 1414 (1993); W. E White *et al.*, *Opt. Lett.* **18**, 1343 (1993).
35. See, for example, A. Siegman, *Lasers* (University Science Books, Mill Valley, CA, 1986), p. 282.
36. F. Salin, C. Rouyer, J. Squier, S. Coe, G. Mourou, *Opt. Commun.* **84**, 67 (1991).
37. B. Stuart, S. Herman, M. D. Perry, in preparation.
38. B. Boyd *et al.*, in preparation.
39. M. D. Perry *et al.*, U.S. patent, in process.
40. T. S. Luk *et al.*, *Phys. Rev Lett.* **51**, 110 (1983).
41. A. L'Huillier, L. A. Lompré, G. Mainfray, C. Manus, *Phys. Rev. A* **27**, 2503 (1983).
42. M. D. Perry, O. L. Landen, A. Szoke, E. M. Campbell, *Phys. Rev. Lett.* **60**, 1270 (1988); S. Augst, *ibid.* **63**, 2212 (1989).
43. P. Agostini, F. Fabre, G. Mainfray, G Petite, *ibid* **42**, 1127 (1979).
44. P. Kruit, J. Kimman, H. G. Muller, M. J. van der Wiel, *Phys. Rev. A* **28**, 248 (1983).
45. R. R. Freeman *et al.*, *Phys. Rev. Lett.* **59**, 1092 (1987); M. D. Perry, K. C. Kulander, A. Szoke, *ibid.* **63**, 1058 (1989).
46. U. Mohideen *et al.*, *ibid.* **71**, 509 (1993); K. J. Schafer, B. Yang, L. F. DiMauro, K. C. Kulander, *ibid.* **70**, 1599 (1993).
47. K. C. Kulander, *Phys. Rev. A* **38**, 778 (1988).
48. J. H. Eberly, Q. Su, J. Javanainen, *Phys. Rev. Lett.* **62**, 881 (1992).
49. R. M. Potvliege and R. Shakeshaft, *Phys. Rev. A* **40**, 3061 (1989).
50. F. H. M. Faisal, *Theory of Multiphoton Processes* (Plenum, New York, 1987), and references therein.
51. M. D. Perry, O. L. Landen, J. Weston, R. Ettlebrick, *Opt Lett.* **14**, 42 (1988).
52. T. S. Luk *et al.*, *J. Opt. Soc. Am. B* **4**, 847 (1987).
53. K. C. Kulander and B. W. Shore, *Phys. Rev. Lett.* **62**, 524 (1989); K. J. Schafer, J. L. Krause, K. C. Kulander, *Int. J. Nonlinear Opt. Phys.* **1**, 245 (1992).
54. J. F. Reintjes, *Nonlinear Optical Parametric Processes in Liquids and Gases* (Academic Press, Orlando, FL, 1984).
55. J. J. Macklin, J. D Kmetec, C. L. Gordon, *Phys. Rev. Lett.* **70**, 766 (1993).
56. J. K. Crane, H. Nguyen, M. D. Perry, in preparation.
57. J. L. Krause, K. J. Schafer, K. C Kulander, *Phys. Rev. Lett.* **68**, 3535 (1992).
58. M. D. Perry and J. K. Crane, *Phys. Rev. A* **48**, 4051 (1993).
59. J. K. Crane, M. D. Perry, D. Strickland, R Falcone, *IEEE Trans. Plasma Sci.* **21**, 82 (1993).
60. A. L'Huillier, P. Balcou, S. Candel, K. J. Schafer, K. C. Kulander, *Phys. Rev. A* **46**, 2778 (1992); A. L'Hullier, K. Schafer, K. C. Kulander, *J. Phys. B* **24**, 3315 (1991).
61. P. Saliere, A. L'Huillier, T. Ditmire, K. S. Budil, M. D. Perry, *J. Phys. B* **27**, 11 (1994).
62. T Ditmire, J. K. Crane, H. Nguyen, M. D. Perry, in *Ultrafast Phenomena IX*, G. Mourou and A. Zewail, Eds. (Optical Society of America, Washington, DC, 1994).
63. P. Balcou *et al.*, *Opt. Lett*, in press
64. H. Hamster, A. Sullivan, S. P. Gordon, W. White, R. W. Falcone, in *Physics With Intense Laser Pulses*, M. D. Perry and P B. Corkum, Eds. (Optical Society of America, Washington, DC, 1993), vol. V.
65. P. Sprangle, E. Esarey, A. Ting, G Joyce, *Appl. Phys. Lett.* **53**, 2146 (1988).
66. C. B. Darrow *et al.*, *Phys. Rev. Lett.* **69**, 442 (1992).
67. J. C. Kieffer *et al.*, *ibid.* **68**, 480 (1992).
68. W. Priedhorsky, D Lier, R. Day, D Gerke, *ibid.* **47**, 1661 (1981).
69. J. Kmetec *et al.*, *ibid.* **68**, 1527 (1992).
70. C. B. Darrow, S. M Lane, D. Klem, M. D. Perry, in preparation.
71. X. Liu and D. Umstadter, *Phys. Rev. Lett.* **69**, 1935 (1992).
72. O. Peyrusse, J. C. Kieffer, C. Y. Côté, M. Chaker, *J. Phys. B* **26**, 511 (1993).
73. J. C. Kieffer *et al.*, *Phys. Fluids B* **5**, 2676 (1993).
74. J. D. Lindl, E M. Campbell, R. L McCrory, *Phys. Today* **45** (no. 9), 32 (1992), G. Taubes, *Science* **262**, 1504 (1993).
75. M Tabak *et al*, *Phys. Rev. Lett.*, in press
76. G B. Zimmerman and W. L. Kruer, *Comments*

Plasma Phys. Controlled Fusion **2**, 85 (1975).
77. F. Salin, J. Squier, G. Mourou, G. Vallancourt, *Opt. Lett.* **16**, 1964 (1991); T. B. Norris, *ibid.* **17**, 1009 (1992).
78. We thank our many colleagues for helpful discussions leading to this article, particularly P. Bucksbaum, E. M. Campbell, J. K. Crane, C. Darrow, R. Falcone, J. C. Kieffer, H. Powell, M. Tabak, and J. Woodworth. Supported by the U.S. Department of Energy under contract W-7405-Eng-48 and the National Science Foundation, Center for Ultrafast Studies.

Sex Determination and Dosage Compensation: Lessons from Flies and Worms

Susan M. Parkhurst and Philip M. Meneely

In both *Drosophila melanogaster* and *Caenorhabditis elegans* somatic sex determination, germline sex determination, and dosage compensation are controlled by means of a chromosomal signal known as the X:A ratio. A variety of mechanisms are used for establishing and implementing the chromosomal signal, and these do not appear to be similar in the two species. Instead, the study of sex determination and dosage compensation is providing more general lessons about different types of signaling pathways used to control alternative developmental states of cells and organisms.

Sex determination is a particularly appealing model system in which to study developmental biology because the developmental decision is made between only two alternative states, male or female, each of which is viable and easily identifiable even within a single cell or a small group of cells. The sum of these individual cellular decisions in the soma, referred to as somatic sex determination, is seen in the whole organism as the morphological differences between male and female. There are also differences in germline sex determination that give rise to either sperm or oocytes and, in levels of X-linked gene expression, a process called dosage compensation.

Although other signals, including environmental cues, are used as a signal in some organisms, the signal for sex determination and dosage compensation in *Caenorhabditis elegans*, *Drosophila melanogaster*, and in mammals is chromosomal. The overall strategy for mammalian sex determination appears to be relatively simple: the phylogenetically conserved *Tdy* (testes-determining on Y) locus, identified on the Y chromosome, acts as a positive signal for testes development and subsequent male sexual differentiation (*1*, *2*). In an apparently independent event, the organism recognizes the number of X chromosomes and inactivates all but one in order to achieve dosage compensation in females (*3*).

In contrast to mammals, the chromosomal signal for sex determination and dosage compensation in *Drosophila* and *C. elegans* is considerably more elaborate. The Y chromosome is not an important signal in *Drosophila* in which males are XY and is not even present in *C. elegans* in which males are normally X0. Instead, the chromosomal signal is the ratio of the number of X chromosomes to the number of sets of autosomes, referred to as the X:A ratio (*4*). Normal animals are diploid, that is, have two sets of autosomes (A = 2). Because females have two X chromosomes, their X:A ratio is 1, whereas males with one X chromosome have an X:A ratio of 0.5. The signal from the X:A ratio is implemented by a hierarchy of a small number of genes that function to control somatic sex differentiation, germline sex determination, or X-chromosome dosage compensation. In recent years, molecular and genetic studies have increased our understanding of the means by which the signal from the X:A ratio is established, maintained, and transmitted to downstream effector genes. In this article, we summarize recent progress in sex determination and dosage compensation in *C. elegans* and *Drosophila* and compare sex determination and dosage compensation in these organisms to these processes in mice and humans.

The authors are with the Division of Basic Sciences, Fred Hutchinson Cancer Research Center, Seattle, WA 98104, USA.

Somatic Sex Determination

One of the first tasks of a fly embryo is to assess its chromosomal constitution. Transduction of this X:A signal activates a key regulatory gene, *Sex-lethal* (*Sxl*), that in turn regulates the choice between the female and male developmental pathways (*5*). The sex determination decision is cell-autonomous: the decision is stably and independently made by single cells. *Sxl* also regulates dosage compensation to increase X-linked gene expression in males that have only one X chromosome to the same level as that of females that have two X chromosomes. Intermediate X:A ratios yield intersex flies whose tissues are mosaics of male and female cells. Females require continuous *Sxl* activity for proper sexual development, whereas males do not require *Sxl*. Both the lack of *Sxl* expression in females or the constitutive expression of *Sxl* in males results in sex-specific lethality because of inappropriate X-chromosome dosage compensation.

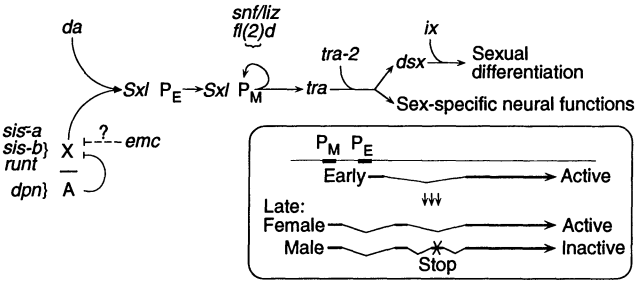

Fig. 1. Summary of the genes and their interactions governing somatic sex determination in *Drosophila*. The primary signal for sex determination is the X:A ratio. Three genes that assess the X component of this ratio (*sis-a*, *sis-b*, and *runt*) work in conjunction with the Da protein to initiate *Sxl* expression at its early promoter, *Sxl* P_E. Two negatively acting factors, one assessing the autosomal component of the X:A ratio, *dpn*, and a maternally required gene, *emc*, inhibit the activity of the X counting elements. Once *Sxl* expression is initiated, a positive autoregulatory feedback loop is established through its late, maintenance promoter, *Sxl* P_M. The products of the *snf/liz* and *fl(2)d* genes appear to be involved in setting up this autoregulatory pathway. Active SXL protein then directs a cascade of sex-specific splicing interactions that culminates in the transcriptional regulation of target differentiation genes that specify male or female morphogenetic products. The inset shows the relation of the *Sxl* P_E and *Sxl* P_M promoters. (Only the splicing for relevant exons is shown.) Early transcripts from the *Sxl* P_E promoter are produced in animals with a high X:A ratio. These transcripts are spliced to yield full-length active SXL protein that in turn is needed for productive splicing of the late transcript in females. Because males do not accumulate full-length active SXL protein from the *Sxl* P_E promoter, they do not exclude an exon containing a stop codon and produce truncated, inactive protein. It is not known how the early transcripts from the *Sxl* P_E promoter are spliced productively in the initial absence of active SXL protein.